Structural evolution of the Fe-Si binary system under extreme pressure

Bingxin Wu, Zepeng Wu, Peng Chen, Nan Huang, Tie-Yu Lü, Xinrui Cao, Yang Sun, Zi-Zhong Zhu, and Shunqing Wu*

Department of Physics, OSED, Key Laboratory of Low Dimensional Condensed Matter Physics (Department of Education of Fujian Province), Xiamen University, Xiamen 361005, China

(Received 10 September 2025; accepted 9 February 2026; published 2 March 2026)

The stability of Fe-Si compounds under extreme pressure is critical for understanding the composition and evolution of Earth's core and terrestrial planetary interiors. Using first-principles calculations and adaptive genetic algorithm crystal structure prediction method, we systematically investigated the thermodynamic stability of Fe-Si compounds and their structural evolution as a function of silicon concentration over pressures ranging from 0 GPa to 1 TPa. At 0 K, B2-FeSi is identified as the sole thermodynamically stable phase at high pressures. Through structural characterization analysis of metastable structures, we found that as the Si content increases, there is a transition in structural motifs from hcp to bcc and then to fcc. Furthermore, electronic and vibrational entropies significantly enhance the thermodynamic stability of certain alloy structures. Our study highlights the synergistic effects of composition, pressure, and volume in regulating phase stability, providing theoretical insights into the composition and structural evolution of planetary cores.

DOI: 10.1103/vpqh-b5qq

I. INTRODUCTION

The Earth's core is primarily composed of iron with a small amount of nickel. Seismic data indicates that its density is significantly lower than that of pure iron under the core pressure and temperature conditions [1–4], implying the presence of approximately 10% by weight of lighter elements such as silicon, sulfur, oxygen, carbon, and hydrogen [5–7]. These light elements play a crucial role in influencing the core's physical properties, such as density and seismic wave velocity, as well as its dynamic behavior, including magnetic field generation and convection patterns [5,8]. Silicon, in particular, has garnered significant interest due to its unique role in geochemistry and cosmochemistry. Its presence in iron meteorites and its scarcity in the mantle imply that silicon could be the most prevalent light element in the core, with an estimated concentration of up to 14 atomic percent [9]. Theoretical research suggests that adding silicon can account for the notable decrease in core density compared to pure iron and helps explain the density variation between the inner and outer core [10]. Additionally, understanding how silicon behaves during the Earth's formation and the differentiation between the core and mantle offers valuable insights into planetary formation processes [10,11].

Terrestrial planets are rocky planets with internal structure and compositions similar to that of Earth. They are primarily composed of rock and metal, possess solid surfaces, and are typically found in the inner regions of a star system [12]. These planets can also exhibit geological activity, including volcanic eruptions and seismic events. Generally, their mass and size are smaller compared to gas giants, and some may contain a metallic core (primarily iron), a silicate mantle, and a crust, along with a potential atmosphere [13]. The presence of silicon in the universe and its influence on the thermal and mechanical properties of iron alloys indicate that silicon may play a significant role as an alloying element in the Earth's core and the interiors of rocky planets [14,15]. The compounds formed under the high-temperature and high-pressure conditions present on Earth and other terrestrial planets are more complex than those formed at standard temperature and pressure. In some rocky planets with masses reaching three times that of Earth, the internal central pressure may exceed the terapascal (TPa) scale [16,17]. Furthermore, past astronomical observations have already discovered a series of rocky planets with masses reaching up to seven times that of Earth [18,19], such as CoRoT-7b and Kepler-10b. The pressure at the center of these planets likely exceeds 1 TPa [16,17]. Therefore, determining the phase stability and physical properties of Fe-Si alloys at such high pressures is crucial for advancing our understanding of the nature and evolution of planetary interiors. Nevertheless, the investigation of the physical properties of iron-silicon alloys under such conditions continues to pose major experimental challenges, primarily due to the difficulties in replicating the precise pressure-temperature conditions of planetary interiors in laboratory settings [8]. Some experimental researches suggested that the Fe-Si system may exhibit multiphase characteristics, with hexagonal close-packed (hcp), body-centered cubic (bcc), B2 (CsCl-type cubic phase), and liquid phases coexisting at 200–1300 GPa [20–24]. The precise locations of phase boundaries of Fe-Si systems remain unresolved [9,25–30].

Crystal structure prediction (CSP) is a valuable method for identifying new materials and exploring phase space [31,32], with the goal of finding stable or metastable structures under specific conditions such as pressure or temperature [33–36]. Zhang and Oganov conducted a comprehensive analysis of

*Contact author: wsq@xmu.edu.cn

the stability of Fe-Si compounds under the pressure conditions close to the Earth's inner core [37], utilizing the evolutionary crystal structure prediction method known as USPEX. They discovered that FeSi, which is stable at atmospheric pressure (space group $P2_13$), transitions to the B2 structure when pressures exceed 20 GPa, with B2-FeSi remaining stable up to core pressures [37]. Niu *et al.* investigated the high-temperature structural stability of Fe-Si compounds under pressures of up to 500 GPa by employing particle swarm optimization algorithms (CALYPSO) and the quasiharmonic approximation (QHA) [38]. Their findings revealed that among all the Fe-Si candidate compounds, only B2-FeSi remains thermodynamically stable at high pressure. In recent years, machine learning methods have made significant advances in the field of materials simulation [39–42], particularly through the development of machine learning potentials. For example, a recent study based on such potentials has determined the phase diagram of iron-rich regions in the Fe-Si system under Earth's core pressures [43]. However, the stable phases of the Fe-Si system at higher pressures and the influence of silicon concentration on structural phase transitions in Fe-Si alloys remain unexplored.

In this context, the adaptive genetic algorithm (AGA) method [35] provides an efficient and accurate CSP framework by combining rapid structural exploration with classical potentials and iterative refinement via first-principles calculations. The AGA method has been successfully applied to a wide range of intermetallic and planetary interior systems [44–48], including our previous studies. Building on this approach, we performed a systematic investigation of the Fe-Si binary system up to ∼1 TPa, representative of terrestrial planetary core conditions. Our analysis emphasizes the evolution of structural motifs as a function of silicon content and further considers the role of electronic and vibrational entropies in stabilizing Fe-Si phases.

II. COMPUTATIONAL METHODS

The AGA crystal structure prediction method [35] was employed to predict the structures of Fe-Si compounds. In this work, an accelerated structure exploration was achieved by combining a classical auxiliary potential with adaptive, iterative first-principles refinement. The initial population for the genetic algorithm (GA) search consisted of 128 randomly generated structures without any predefined lattice symmetry. Throughout the GA search, the population size was maintained at 128. After local relaxation to the nearest energy minimum, all structures were ranked according to their enthalpies. In each GA generation, 32 new candidate structures (one quarter of the population) were produced from the parent pool using the mating scheme described in Ref. [49], and these offspring replaced the 32 highest-enthalpy structures to form the next generation. The structural exploration employing the auxiliary interatomic potential was carried out for 500 consecutive GA generations.

Following the AGA scheme described in Ref. [35], the 16 lowest-enthalpy structures at the end of each GA search were selected for single-point DFT calculations. The resulting energies, forces, and stresses were then used to refine the parameters of the interatomic potential for the subsequent GA cycle. A total of 40 adaptive iterations were performed to obtain the final structures. In the GA searches, an embedded-atom method (EAM) potential [50] was adopted as the auxiliary classical potential. The potential was fitted using the force-matching method combined with stochastic simulated annealing, as implemented in the POTFIT code [51].

Our first-principles calculations were conducted by using the Vienna *Ab initio* Simulation Package (VASP) [52], which implements the Projector Augmented Wave (PAW) [53] method. The exchange-correlation energy was treated with the spin-polarized Generalized Gradient Approximation (GGA) using the Perdew-Burke-Ernzerhof (PBE) [54] functional. Only ferromagnetic configurations were considered. To account for potential net magnetic moments in the system and to test for Fe-induced magnetic moments on Si atoms, we initialized the magnetic moments of Fe and Si to $5\mu_B$ and $3\mu_B$, respectively, ensuring the robustness of the calculations. The electron configurations employed in our calculations are $3d^74s^1$ and $3s^23p^2$ for Fe and Si. The calculation settings included a specified plane wave cutoff of 400 eV, and the Monkhorst-Pack [55] scheme for Brillouin zone sampling with a k-point resolution of $2\pi \times 0.025$ Å^{-1}. We also tested a harder pseudopotential and a higher energy cutoff. As shown in Fig. S1 [56], the results confirm that the chosen pseudopotential and energy cutoff can reliably describe the relative enthalpy and structural stability of the Fe-Si system over the high-pressure range from 100 GPa to 1 TPa. During structural relaxation, the atomic force convergence threshold was 0.01 eV/Å. These parameters were thoroughly tested and demonstrated to be sufficient for achieving well-converged total energy results.

The thermodynamic stability of $Fe_{1-x}Si_x$ was assessed by computing the formation enthalpies H_f, which is defined as $H_f = H_{Fe_{1-x}Si_x} - (1-x)H_{Fe} - xH_{Si}$, where $H_{Fe_{1-x}Si_x}$ is the enthalpy per atom of phase $Fe_{1-x}Si_x$ and H_{Fe} (H_{Si}) is the enthalpy per atom of the stable phase of Fe (Si) under the corresponding pressure. The reference states of the pure Fe and Si at each pressure are selected as follows: The ground state of Fe is chosen as the ferromagnetic body-centered cubic (FM-bcc, space group $Im\bar{3}m$) phase at 0 GPa and the hexagonal close-packed (hcp, space group $P6_3/mmc$) phase when higher than 100 GPa [57]. The ground state of Si is the diamond structure (space group $Fd\bar{3}m$) at 0 GPa, and the face-centered cubic structure (fcc, space group $Fm\bar{3}m$) when higher than 100 GPa [58,59].

The structural motifs were analyzed using the Polyhedral Template Matching (PTM) method in OVITO software [60]. PTM identifies the local crystal structure of atoms by matching their neighborhoods with predefined structural templates. For each atom, PTM attempts to map the neighborhood onto every candidate template. When a match exists, the Root-Mean-Square Deviation (RMSD) is computed, and the template with the lowest RMSD is assigned to that atom. The candidate templates are hcp, bcc, and fcc. We adopted an RMSD cutoff of 0.15.

The finite displacement method was used to evaluate the dynamical stability of Fe-Si phases. Supercells containing ∼128 atoms were constructed, with a uniform Γ-centered k-point mesh of density $2\pi \times 0.025$ Å^{-1}. The second-order force constants and harmonic phonon dispersion curves were

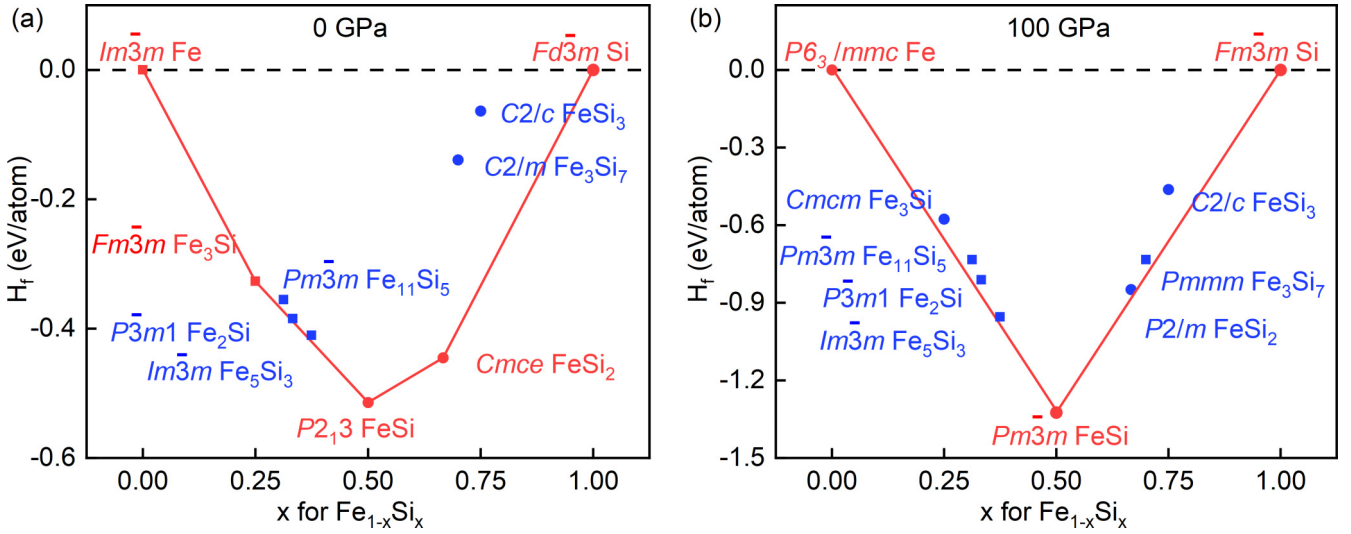

FIG. 1. The convex hull of the Fe-Si system at (a) ambient pressure and (b) 100 GPa. Circles and squares represent nonmagnetic structures and ferromagnetic structures, respectively. Red and blue symbols indicate thermodynamically stable structures and metastable structures, respectively. The structures are all from previous studies [38,63–67] and their crystal structures are as shown in Fig. S2 [56].

obtained using the PHONOPY code [61]. Thermodynamic properties at finite temperatures were investigated within the QHA [62].

III. RESULTS AND DISCUSSION

A. Thermodynamic stability and compositional evolution of the Fe-Si system

Given the geophysical importance of Fe-Si alloys, it is crucial to evaluate their phase stability under compression. We first evaluated the thermodynamic stability of known Fe-Si binary compounds over a pressure range from 0 to 100 GPa. As shown in Fig. 1(a), there are three thermodynamically stable phases at 0 GPa, which are $Fm\bar{3}m$ Fe_3Si, $P2_13$ FeSi, and $Cmce$ $FeSi_2$. This is consistent with the results from Oganov [37]. With pressure increasing into 100 GPa, there is only one thermodynamically stable phase, i.e., B2-FeSi (space group $Pm\bar{3}m$). The former Fe_3Si phase tends to decompose into hcp-Fe and B2-FeSi, and $FeSi_2$ decomposes into B2-FeSi and fcc-Si.

In order to explore the possible low-enthalpy structures of the Fe-Si system at higher pressure, we conducted a structural search on common proportions of Fe_xSi_y ($x = 1$, $y = 1, 2, 3$; $x = 2, 3$, $y = 1$; $x = 5$, $y = 3$; $x = 4$, $y = 1$; $x = 11$, $y = 5$); then we carried out supplementary work in the iron-rich and silicon-rich regions ($x = 1$, $y = 7, 11, 13, 15$; $x = 2$, $y = 11, 12, 13$; $x = 3$, $y = 5, 7,13$; $x = 5$, $y = 1, 11$; $x = 7$, $y = 1, 9$; $x = 4$, $y = 6, 8, 9, 15$). The largest simulation unit cell comprised up to 40 atoms. We firstly performed AGA search simulations at 400 GPa. Besides, we found that most of metastable structures at 100 GPa have the body-centered cubic-like (bcc-like) framework, see in Fig. S2 [56]. These results suggest that the bcc framework is the preferred structure of Fe-Si alloy at high pressure. Therefore, we constructed a series of Fe-Si bcc solid solution structures as candidates. We constructed three 16 iron atoms bcc supercells using different supercell expansions ($2 \times 2 \times 2$, $4 \times 2 \times 1$, $8 \times 1 \times 1$) and performed the sequential substitution with silicon, ranging from 1 to 16 atoms. Following structural deduplication, 4573 structures were retained. The relative enthalpies of all the substitutional compounds with H_d less than 0.6 eV/atom at 400 GPa were shown in Fig. 2(a). It is clear that under high-pressure conditions, while numerous metastable compounds exist in the Fe-Si system, the B2-type FeSi remains the sole stable phase. By examining an energy range of 100 meV/atom above convex hull, corresponding to a thermal energy of approximately 1160 K, we discovered that the configurations within this range all exhibit basic bcc, fcc, and hcp motif structures by PTM analysis. To explore the potentially stable structures at higher pressure, we also performed AGA research at 1 TPa. As shown in Fig. 2(b), even at this high-pressure level, the Fe-Si system remains with only one stable phase, the B2-type FeSi. For 1 TPa, we selected an energy range of 150 meV/atom above convex hull, corresponding to a thermal energy of approximately 1740 K. Upon examining the structures within this energy range, we observe that at these low-energy structures continue to exhibit basic bcc, fcc, and hcp motifs. No special mixed coordination environments, such as those observed in SiO_2 under high pressure [68], were found. To contextualize our theoretical predictions with experimental findings, we selected a metastable structure, $C2/m$ Fe_3Si, with Si content similar to that used in the shock-compression experiment [24] and compared the calculated density-pressure relationship with the experimental measurements, as shown in Fig. S3 [55]. The slope of the density-pressure curve for our predicted $C2/m$ Fe_3Si phase shows strong agreement with the experimental trend for Fe-15 wt.% Si over the pressure range of 100 GPa to 1 TPa. The discrepancy in absolute values may primarily stem from the high-temperature conditions of the experiment.

In order to reveal the relationship between silicon concentration and structural characteristics, we employed PTM to analyze all Fe-Si structures and quantified the fraction of hcp, bcc, and fcc motifs in each structure. Assuming that there are M atoms with the local crystal structure of fcc in

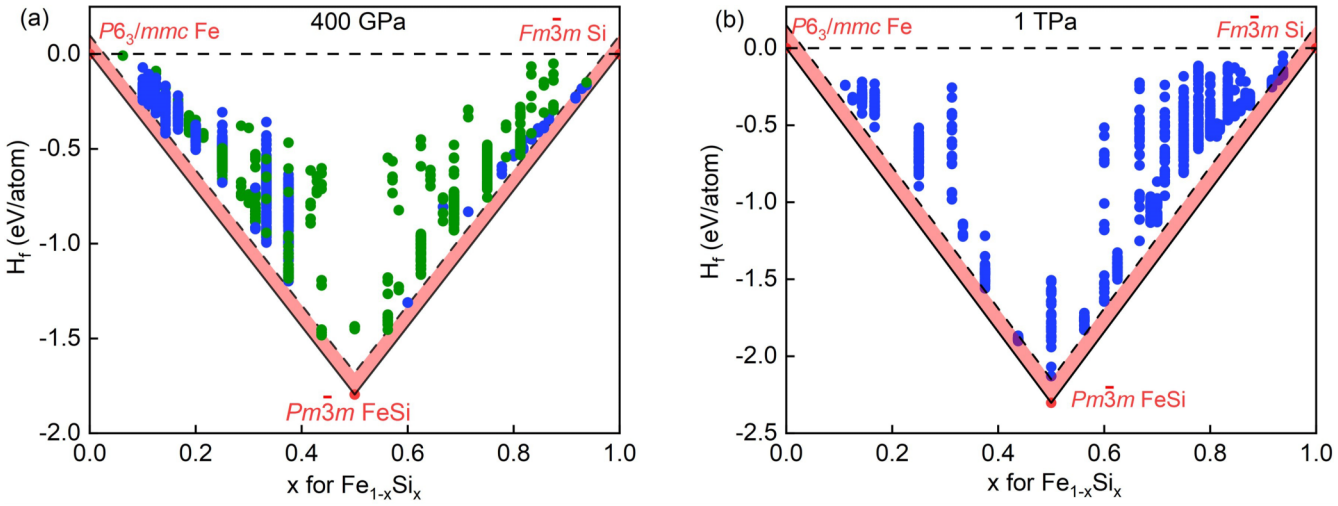

FIG. 2. The convex hull of Fe-Si compounds at (a) 400 GPa and (b) 1 TPa. The green dots represent the structures obtained by bcc substitution, the blue dots represent the structures obtained through AGA search, and the thermodynamically stable phases are highlighted by red dots. The red shaded area corresponds to the energy band: 0.1 eV/atom for 400 GPa, and 0.15 eV/atom for 1 TPa.

a certain Fe-Si compound with N atoms, then the percentage of fcc is calculated as $\frac{M}{N} \times 100\%$. Similarly, the percentages of bcc and hcp can be obtained, while treating the fractional coordinates corresponding to the fcc, bcc, and hcp motifs as the red, green, and blue components, respectively. As shown in Fig. 3(a), by analyzing the lower-energy structures for each composition, the structural motifs of the Fe-Si system show a distinct relationship with silicon concentration (x_{Si}) at 400 GPa, which can be categorized into three specific ranges. At low silicon concentrations ($0 < x_{\mathrm{Si}} < 0.25$), the Fe-Si system predominantly exhibits an hcp-like structure, analogous to that of pure iron. In the medium silicon range ($0.25 < x_{\mathrm{Si}} < 0.675$), the structure is mainly bcc-like, resembling the B2-FeSi phase. At high silicon concentrations ($0.675 < x_{\mathrm{Si}} < 1$), the system tends to adopt an fcc-like structure, similar to that of pure silicon. Similarly, at 1 TPa, the structural motifs of the Fe-Si system also exhibit a significant dependence on silicon concentration, as shown in Fig. 3(b). The boundaries of the three characteristic regions remain nearly unchanged, indicating that these boundaries are weakly influenced by variations of pressure.

B. The pressure dependence of the phase stability in Fe-Si compounds

Having clarified the compositional dependence of phase stability, we next investigate how pressure modifies the energy landscape of Fe-Si compounds. This step allows us to connect the observed structural motifs with their energetic origins under varying pressure conditions. To investigate the variation of energy in the Fe-Si system under increasing pressure, we performed a detailed analysis of the relative energy changes across different stoichiometric ratios. Figure 4 shows the evolution of the enthalpy above the convex hull (H_d) as a function

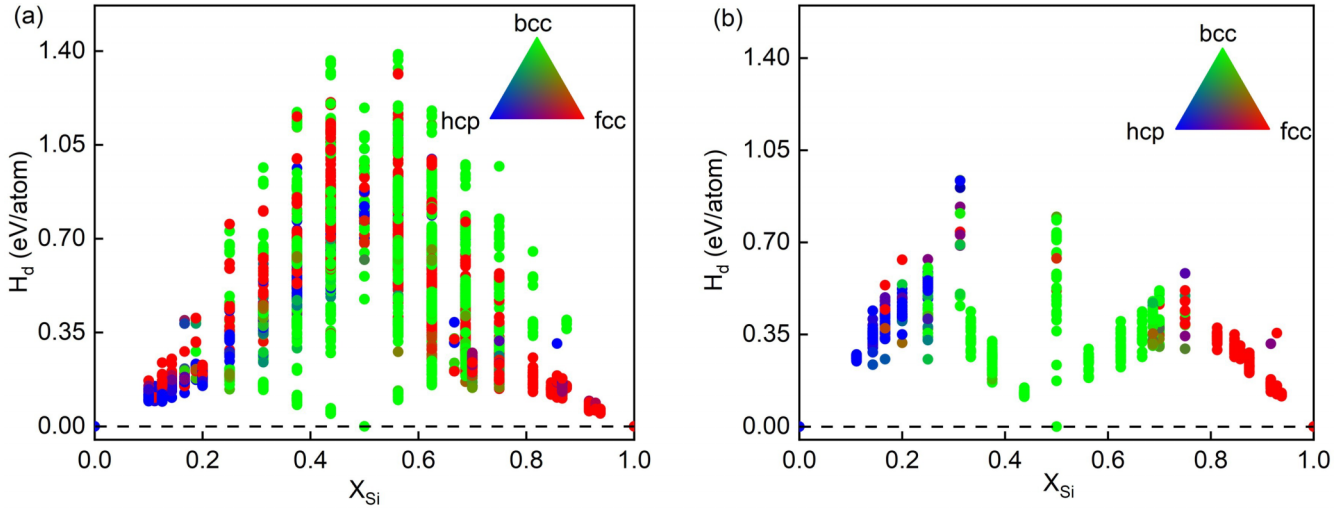

FIG. 3. The enthalpy above convex hull, H_d, of Fe-Si compounds as a function of Si concentration at (a) 400 GPa and (b) 1 TPa, with color mapping representing the structural order parameter, where the RGB components correspond to the percentages of fcc, bcc, and hcp structures, respectively.

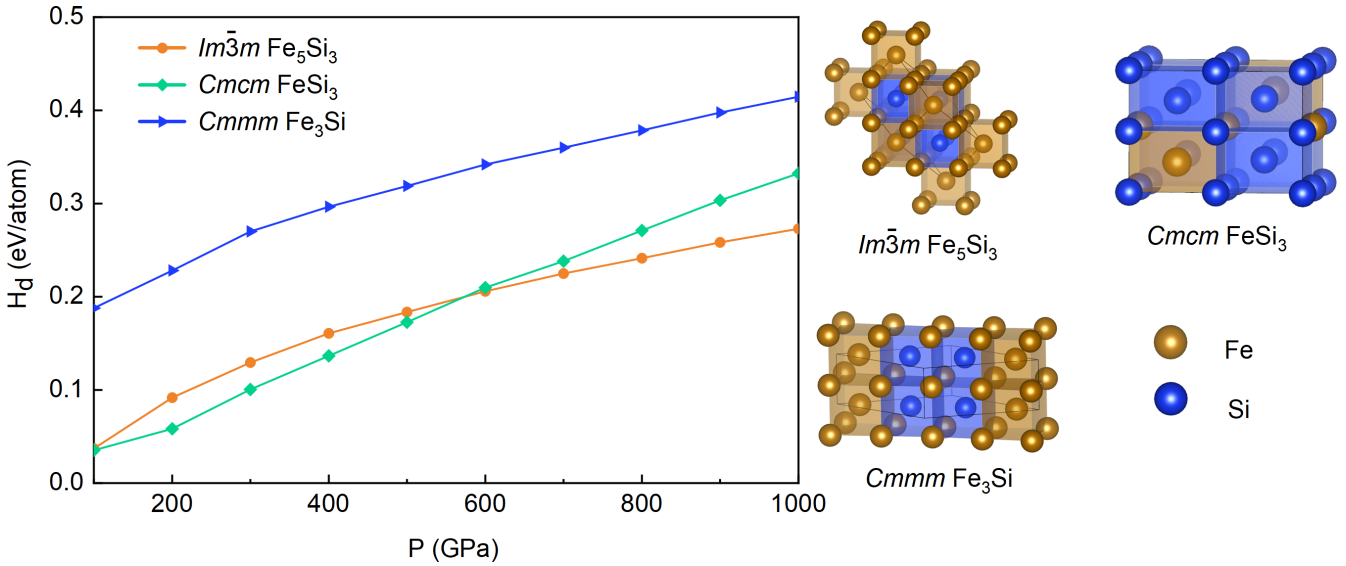

FIG. 4. Variation of the enthalpy above the convex hull for representative Fe-Si compounds as a function of pressure.

of pressure for representative low-energy structures identified by the AGA search, alongside several known structures, over the pressure range from 100 GPa to 1 TPa. The results indicate that Fe-Si compounds (including Fe_5Si_3, $FeSi_3$, and Fe_3Si) exhibit increasing H_d values with rising pressure.

To elucidate the thermodynamic driving forces stabilizing B2-FeSi, we examined the enthalpy as a function of volume for various Fe-Si phases. As shown in Fig. 5(a), the volume of pure silicon exceeds that of pure iron at 400 GPa. It would be expected that increasing the Si concentration in Fe-Si compounds leads to an increase in volume. However, for silicon concentrations between 0.375 and 0.625, the low-energy Fe-Si compounds exhibit unexpectedly smaller volumes, deviating from the anticipated trend of volume expansion with higher silicon content. Additionally, we observed that within this range of silicon concentration, a smaller volume corresponds to a lower enthalpy for a given concentration, as depicted in Fig. 5(b), where H_d shows a positive correlation with volume. We analyzed several low-energy structures with moderate silicon concentrations. As shown in Fig. S4 [56], in these structures except B2-FeSi, the formation of either Fe-Fe bonds or Si-Si bonds is inevitable. As these bonds are generally longer than Fe-Si bonds, the resulting structures exhibit a larger volume compared to that of B2-FeSi, in which only Fe-Si bonds are present. At 1 TPa, the volume of pure iron is larger than that of pure silicon (see Fig. S5 [56]). As the silicon concentration increases, the volume of Fe-Si compounds generally decreases. However, for silicon concentrations

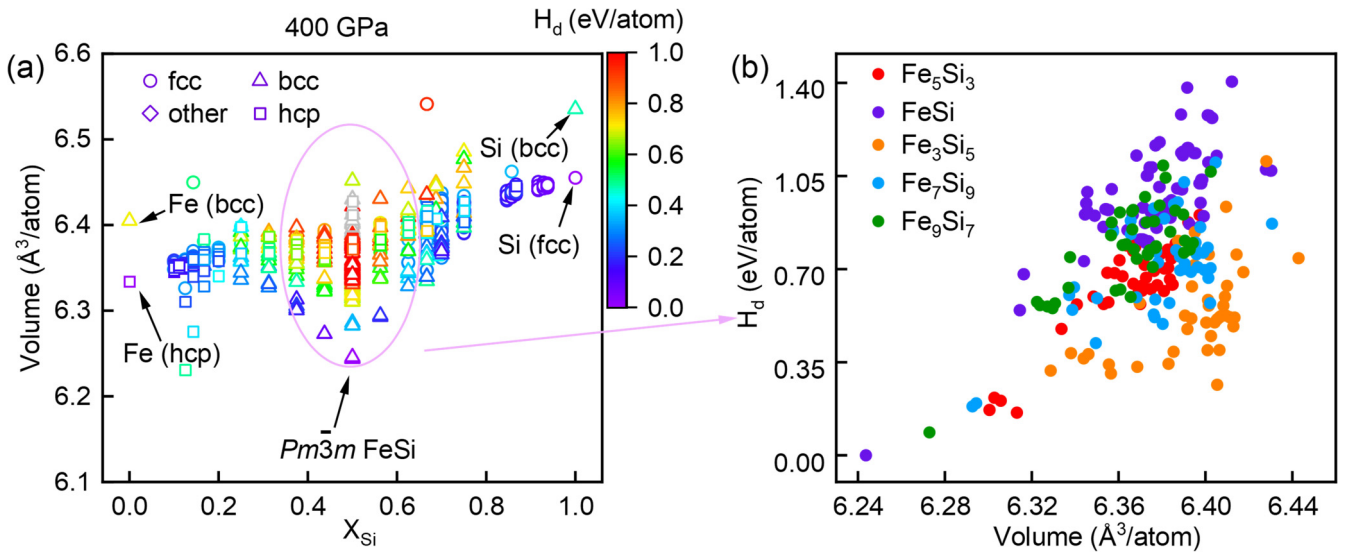

FIG. 5. (a) The volume of Fe-Si compounds as a function of silicon concentration, with color mapping indicating the corresponding H_d. And gray color represents its H_d above 1 eV/atom. Different symbols represent different structural motifs. If the percentage of the fcc motif in a certain structure is greater than 50%, we consider this structure to be fcc. The same applies to bcc and hcp. Circles represent fcc, triangles represent bcc, squares represent hcp, and solid circles indicate that the percentages of the three structural motifs are close. (b) The detailed $H_d - Volume$ plot for several compositions in (a).

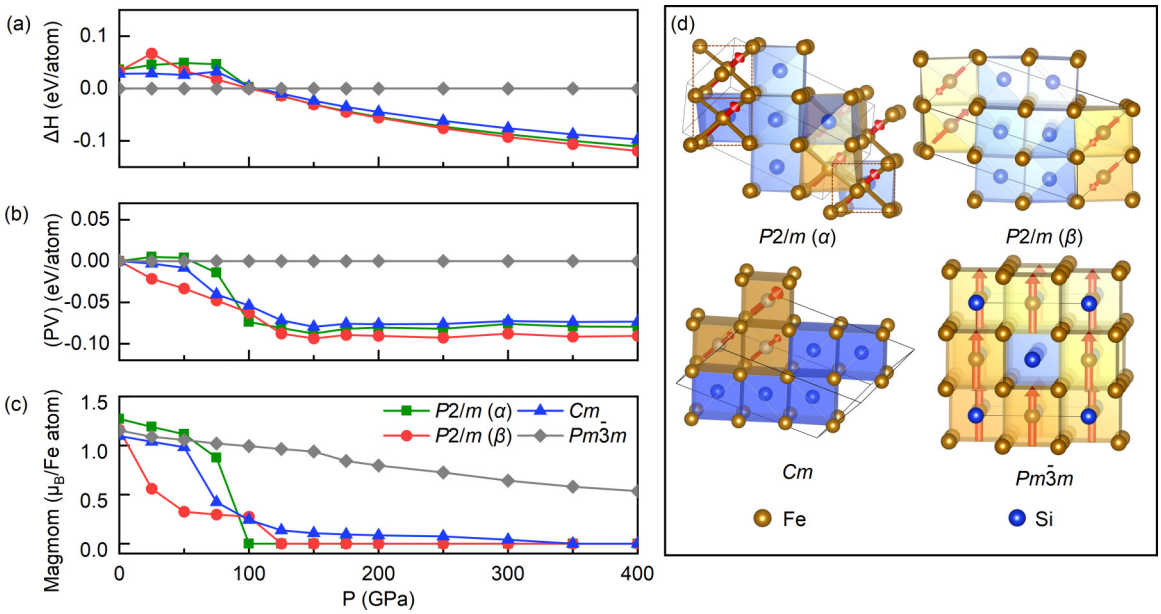

FIG. 6. The (a) enthalpy, (b) volume, and (c) magnetic moment difference between three new phases and the experimental phase with pressure. (d) The crystal structures of the four phases. Red arrows indicate the dominant magnetic moments at 50 GPa. Two *P2/m* phases are distinguished by (α) and (β).

between 0.375 and 0.625, the volume of the low-energy Fe-Si structures was significantly reduced.

C. $Fe_{11}Si_5$ phase at high pressure and high temperature

In addition to the general phase stability trends, it is also important to examine individual compounds that may play a special role at high pressure. Previous experiment indicated that the $Fe_{11}Si_5$ phase at ambient pressure had a space group of $Pm\bar{3}m$ [67], with atoms arranged in a bcc-like structure. As shown in Fig. 6(d), each silicon atom of $Pm\bar{3}m$ $Fe_{11}Si_5$ is located at the center of a cube formed by eight iron atoms, constituting an Si-Fe_8 structural motif. In this study, we identified three new metastable $Fe_{11}Si_5$ phases under high pressure ($P \geqslant 100$ GPa) with lower enthalpies than $Pm\bar{3}m$ $Fe_{11}Si_5$, which were *P2/m* (α), *P2/m* (β), and *Cm* phases. Their structures were as shown in Fig. 6(d). These new phases with smaller volumes are more compressible than $Pm\bar{3}m$ phase, which contributes to their lower enthalpy, see in Figs. 6(a) and 6(b). All the three structures are dynamically stable under high pressure, and their phonon spectra were as shown in Fig. S6 [56].

The overall frameworks of these three new structures retain bcc-like characteristics. However, they differ in the specific occupancy sites of Fe and Si atoms, resulting in varying degrees of structural distortion. In all four structures, silicon atoms occupy the body centers of cubes formed by eight nearest-neighbor Fe atoms. Due to slight distortions caused by structural symmetry, these cubes are not perfectly regular, but on average, each Si atom is coordinated by eight Fe atoms. Our calculation results demonstrate that, across all optimized structures, the magnetic moment of Fe atoms remains substantial, while the final magnetic moment of Si atoms rapidly converges to a value close to zero (less than 0.01 μ_B, which is negligible in numerical terms). All Fe atoms with nonzero magnetic moments are located at the centers of Fe-Fe8 polyhedra. The P2/m (α) phase is distinguished by a configuration where the two magnetic Fe atoms reside at the centers of intersecting Fe-Fe8 polyhedra. In this arrangement, one Fe atom sits at a vertex of the polyhedron centered on the other. With the pressure increasing, *P2/m* (α), *P2/m* (β), and *Cm* phases are nonmagnetic, and only the $Pm\bar{3}m$ $Fe_{11}Si_5$ phase retains its magnetism. To elucidate the effect of high pressure on the magnetism of various $Fe_{11}Si_5$ phases, we calculated the evolution of their electronic structures under non-spin-polarized conditions and performed an analysis based on the Stoner [69] criterion. As shown in Fig. S7 [56], at ambient pressure, all four phases exhibit a high density of state (DOS) at the Fermi level ($N(E_F)$), suggesting the possible occurrence of spin polarization according to the Stoner criterion. When the pressure is increased to 400 GPa, the $N(E_F)$ values of the *Cm*, *P2/m* (α), and *P2/m* (β) phases decrease to approximately 1 states/(eV Fe). In contrast, the $Pm\bar{3}m$ phase maintains an $N(E_F)$ value greater than 1 states/(eV Fe), implying the persistence of spin polarization. This inference is further corroborated by spin-polarized calculations.

It is widely accepted that the Earth's core contains silicon as a light element in iron [9]. However, there remains considerable debate regarding both the exact silicon content and whether Fe-Si alloys adopt a bcc [70,71] or an hcp [72,73] structure under core conditions. Therefore, investigating the stability trends of Fe-rich Fe-Si alloys at high temperatures and high pressures is of great significance for resolving these controversies and advancing our understanding of the Earth's core. To further study the thermodynamical stability of these phases at finite temperatures, we initially investigated the effect on the thermodynamic stability of electronic entropy. Here, we take $Fe_{11}Si_5$ as an example and further discuss the

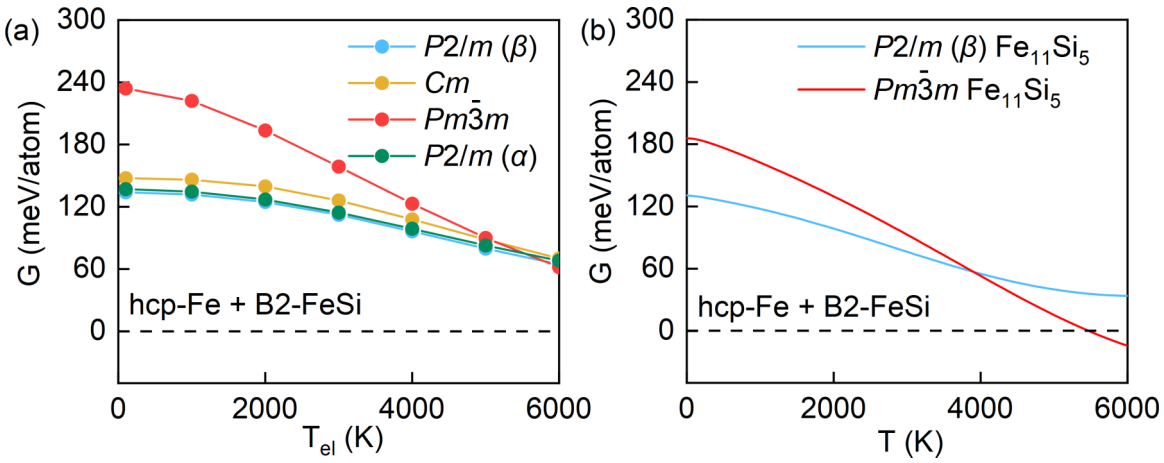

FIG. 7. (a) Relative Gibbs free energy with only electronic entropy for the four phases of $Fe_{11}Si_5$ at 200 GPa. (b) Relative Gibbs free energy with electronic entropy and vibration entropy (QHA) for $P2/m$ (β) $Fe_{11}Si_5$ and $Pm\bar{3}m$ $Fe_{11}Si_5$ at 200 GPa. The reference systems are hcp-Fe and B2-FeSi.

influence of temperature on its stability at 200 GPa. The electronic entropy was included using the Mermin functional [74]. As shown in Fig. 7(a), electronic entropy significantly reduces the relative Gibbs free energies for all four alloy phases of $Fe_{11}Si_5$. Among them, the free energy of the $Pm\bar{3}m$ phase decreases most significantly with increasing electronic temperature. And the magnetic moment of $Pm\bar{3}m$ phase decreased with electronic temperature increasing, as shown in Fig. S8 [56]. Furthermore, we focused on two lower-energy phases ($P2/m$ (β) and $Pm\bar{3}m$) to evaluate the effects of vibrational entropy by QHA. As shown in Fig. 7(b), the results show that the relative Gibbs free energy of the $Pm\bar{3}m$ phase is less than zero at above 5500 K, which indicates $Pm\bar{3}m$ phase is thermodynamically stable at high-temperature conditions. Considering that the melting point of Fe and Fe-Si alloys at 200 GPa may be lower than 5000 K [75,76], the $Pm\bar{3}m$ phase would already be molten at 5500 K. However, we emphasize that both electronic and vibrational entropies contribute to lowering the Gibbs free energy of $Fe_{11}Si_5$ relative to Fe and B2-FeSi. At even higher pressures, we selected the representative phase $Im\bar{3}m$ Fe_5Si_3 and likewise accounted for both electronic and vibrational entropy. As illustrated in the Fig. S9 [56], although Fe_5Si_3 remains in a metastable state, its Gibbs free energy relative to elemental Fe and B2-FeSi is reduced. Furthermore, if anharmonic effects and configurational entropy at high temperatures were taken into account, the metastable $Fe_{11}Si_5$ phase would likely become thermodynamically stable. The discussion on temperature effects suggests that the stability of bcc-structured Fe-Si alloys is enhanced at high temperatures. This stabilization is likely driven by the increased configurational entropy under such conditions, which can facilitate the formation of bcc Fe-Si solid solutions.

IV. CONCLUSIONS

Taken together, these results provide a coherent picture of the structural evolution of the Fe-Si system under extreme conditions. We examined the thermodynamic stability and structural motifs of Fe-Si compounds up to 1 TPa. Our results revealed a phase transition trend in which increasing silicon concentration induces a transformation of structural motifs from hcp to bcc, and subsequently to fcc. Both electronic and vibrational entropies contribute to stabilizing the Fe-Si compounds relative to pure Fe, pure Si, and B2-FeSi. Certainly, future efforts toward precise planetary interior modeling must comprehensively incorporate finite temperature effects. Most metastable Fe-Si phases adopt simple structural frameworks based on hcp, bcc, or fcc lattices, which may facilitate the formation of substitutional solid solutions at high temperatures. Further investigations are needed to confirm this possibility. These results enhance our understanding of the behavior of Fe-Si compounds under high pressure.

ACKNOWLEDGMENTS

This research was supported by National Natural Science Foundation of China (No. 12374015 and No. 42374108). Shaorong Fang and Tianfu Wu from Information and Network Center of Xiamen University are acknowledged for their help with the Graphics Processing Unit (GPU) computing.

DATA AVAILABILITY

The data that support the findings of this article are not publicly available upon publication because it is not technically feasible and/or the cost of preparing, depositing, and hosting the data would be prohibitive within the terms of this research project. The data are available from the authors upon reasonable request.

[1] L. S. Dubrovinsky, S. K. Saxena, F. Tutti, S. Rekhi, and T. LeBehan, *In situ* x-ray study of thermal expansion and phase transition of iron at multimegabar pressure, Phys. Rev. Lett. **84**, 1720 (2000).

[2] O. Anderson and D. Isaak, Another look at the core density deficit of Earth's outer core, Phys. Earth Planet. Inter. **131**, 19 (2002).

[3] J. Shanker, B. Singh, and S. Srivastava, Volume–temperature relationship for iron at 330 GPa and the Earth's core density deficit, Phys. Earth Planet. In. **147**, 333 (2004).

[4] A. Dewaele, P. Loubeyre, F. Occelli, M. Mezouar, P. I. Dorogokupets, and M. Torrent, Quasihydrostatic equation of state of iron above 2 Mbar, Phys. Rev. Lett. **97**, 215504 (2006).

[5] K. Hirose, B. Wood, and L. Vočadlo, Light elements in the Earth's core, Nat. Rev. Earth Environ. **2**, 645 (2021).

[6] J. Li and Y. Fei, Experimental constraints on core composition, in *Treatise on Geochemistry*, 1st ed., edited by H. D. Holland and K. K. Turekian (Pergamon, Amsterdam, 2007), pp. 1–31.

[7] R. McQueen, J. Fritz, and S. Marsh, On the composition of the Earth's interior, J. Geophys. Res. **69**, 2947 (1964).

[8] K. Hirose, S. Labrosse, and J. Hernlund, Composition and state of the core, Annu. Rev. Earth Pl. Sc. **41**, 657 (2013).

[9] D. Alfè, M. Gillan, and G. D. Price, Composition and temperature of the Earth's core constrained by combining *ab initio* calculations and seismic data, Earth Planet. Sci. Lett. **195**, 91 (2002).

[10] T. Liu and Z. Jing, Hydrogen and silicon are the preferred light elements in Earth's core, Commun. Earth Environ. **5**, 282 (2024).

[11] D. C. Rubie, D. J. Frost, U. Mann, Y. Asahara, F. Nimmo, K. Tsuno, P. Kegler, A. Holzheid, and H. Palme, Heterogeneous accretion, composition and core–mantle differentiation of the Earth, Earth Planet. Sc. Lett. **301**, 31 (2011).

[12] J. E. Chambers, Planet formation, in *Treatise on Geochemistry*, 2nd ed., edited by H. D. Holland and K. K. Turekian (Elsevier, Amsterdam, 2014), pp. 55–72.

[13] R. G. Trønnes, M. A. Baron, K. R. Eigenmann, M. G. Guren, B. H. Heyn, A. Løken, and C. E. Mohn, Core formation, mantle differentiation and core-mantle interaction within Earth and the terrestrial planets, Tectonophysics **760**, 165 (2019).

[14] A. Balchan and G. Cowan, Shock compression of two iron-silicon alloys to 2.7 megabars, J. Geophys. Res. **71**, 3577 (1966).

[15] J. Zhang and F. Guyot, Thermal equation of state of iron and Fe 0.91 Si 0.09, Phys. Chem. Miner. **26**, 206 (1999).

[16] F. W. Wagner, F. Sohl, H. Hussmann, M. Grott, and H. Rauer, Interior structure models of solid exoplanets using material laws in the infinite pressure limit, Icarus **214**, 366 (2011).

[17] A. P. van den Berg, D. A. Yuen, K. Umemoto, M. H. Jacobs, and R. Wentzcovitch, Mass-dependent dynamics of terrestrial exoplanets using *ab initio* mineral properties, Icarus **317**, 412 (2019).

[18] A. P. Hatzes, M. Fridlund, G. Nachmani, T. Mazeh, D. Valencia, G. Hébrard, L. Carone, M. Pätzold, S. Udry, and F. Bouchy, The mass of CoRoT-7b, Astrophys. J. **743**, 75 (2011).

[19] F. Wagner, N. Tosi, F. Sohl, H. Rauer, and T. Spohn, Rocky super-Earth interiors-Structure and internal dynamics of CoRoT-7b and Kepler-10b, Astron. Astrophys. **541**, A103 (2012).

[20] H. Huang, C. Leng, Q. Wang, G. Young, X. Liu, Y. Wu, F. Xu, and Y. Fei, Equation of state for shocked Fe-8.6 wt% Si up to 240 GPa and 4,670 K, J. Geophys. Res.: Solid Earth **124**, 8300 (2019).

[21] H. Ozawa, K. Hirose, K. Yonemitsu, and Y. Ohishi, High-pressure melting experiments on Fe–Si alloys and implications for silicon as a light element in the core, Earth Planet. Sc. Lett. **456**, 47 (2016).

[22] R. A. Fischer, A. J. Campbell, D. M. Reaman, N. A. Miller, D. L. Heinz, P. Dera, and V. B. Prakapenka, Phase relations in the Fe–FeSi system at high pressures and temperatures, Earth Planet. Sci. Lett. **373**, 54 (2013).

[23] S. Tateno, Y. Kuwayama, K. Hirose, and Y. Ohishi, The structure of Fe–Si alloy in Earth's inner core, Earth Planet. Sci. Lett. **418**, 11 (2015).

[24] J. K. Wicks, R. F. Smith, D. E. Fratanduono, F. Coppari, R. G. Kraus, M. G. Newman, J. R. Rygg, J. H. Eggert, and T. S. Duffy, Crystal structure and equation of state of Fe-Si alloys at super-Earth core conditions, Sci. Adv. **4**, eaao5864 (2018).

[25] L. Vočadlo, D. Alfè, M. Gillan, I. Wood, J. Brodholt, and G. D. Price, Possible thermal and chemical stabilization of body-centred-cubic iron in the Earth's core, Nature (London) **424**, 536 (2003).

[26] A. S. Côté, L. Vočadlo, and J. P. Brodholt, Light elements in the core: Effects of impurities on the phase diagram of iron, Geophys. Res. Lett. **35**, L05306 (2008).

[27] A. S. Côté, L. Vočadlo, D. P. Dobson, D. Alfè, and J. P. Brodholt, *Ab initio* lattice dynamics calculations on the combined effect of temperature and silicon on the stability of different iron phases in the Earth's inner core, Phys. Earth Planet. In. **178**, 2 (2010).

[28] A. B. Belonoshko, A. Rosengren, L. Burakovsky, D. L. Preston, and B. Johansson, Melting of Fe and $Fe_{0.9375}$ $Si_{0.0625}$ at Earth's core pressures studied using *ab initio* molecular dynamics, Phys. Rev. B **79**, 220102 (2009).

[29] H. Cui, Z. Zhang, and Y. Zhang, The effect of Si and S on the stability of bcc iron with respect to tetragonal strain at the Earth's inner core conditions, Geophys. Res. Lett. **40**, 2958 (2013).

[30] D. Alfe, M. Gillan, and G. Price, Constraints on the composition of the Earth's core from *ab initio* calculations, Nature (London) **405**, 172 (2000).

[31] L. Zhang, Y. Wang, J. Lv, and Y. Ma, Materials discovery at high pressures, Nat. Rev. Mater. **2**, 17005 (2017).

[32] A. R. Oganov, C. J. Pickard, Q. Zhu, and R. J. Needs, Structure prediction drives materials discovery, Nat. Rev. Mater. **4**, 331 (2019).

[33] C. J. Pickard and R. J. Needs, High-pressure phases of silane, Phys. Rev. Lett. **97**, 045504 (2006).

[34] Y. Ma, M. Eremets, A. R. Oganov, Y. Xie, I. Trojan, S. Medvedev, A. O. Lyakhov, M. Valle, and V. Prakapenka, Transparent dense sodium, Nature (London) **458**, 182 (2009).

[35] S. Q. Wu, M. Ji, C.-Z. Wang, M. C. Nguyen, X. Zhao, K. Umemoto, R. Wentzcovitch, and K.-M. Ho, An adaptive genetic algorithm for crystal structure prediction, J. Phys.: Condens. Matter **26**, 035402 (2013).

[36] X. Zhao, M. C. Nguyen, W. Y. Zhang, C. Z. Wang, M. J. Kramer, D. J. Sellmyer, X. Z. Li, F. Zhang, L. Q. Ke, V. P. Antropov, and K. M. Ho, Exploring the structural complexity

of intermetallic compounds by an adaptive genetic algorithm, Phys. Rev. Lett. **112**, 045502 (2014).
[37] F. Zhang and A. R. Oganov, Iron silicides at pressures of the Earth's inner core, Geophys. Res. Lett. **37**, L02305 (2010).
[38] Z.-W. Niu, M. Tang, and L.-C. Cai, Structural stabilities of iron silicides at high pressures and temperatures, Int. J. Mod. Phys. B **34**, 2050119 (2020).
[39] H. Li, Z. Wang, N. Zou, M. Ye, R. Xu, X. Gong, W. Duan, and Y. Xu, Deep-learning density functional theory Hamiltonian for efficient *ab initio* electronic-structure calculation, Nat. Comput. Sci. **2**, 367 (2022).
[40] X. Gong, S. G. Louie, W. Duan, and Y. Xu, Generalizing deep learning electronic structure calculation to the plane-wave basis, Nat. Comput. Sci. **4**, 752 (2024).
[41] Y. Li, Z. Tang, Z. Chen, M. Sun, B. Zhao, H. Li, H. Tao, Z. Yuan, W. Duan, and Y. Xu, Neural-network density functional theory based on variational energy minimization, Phys. Rev. Lett. **133**, 076401 (2024).
[42] H. Li, Z. Tang, J. Fu, W.-H. Dong, N. Zou, X. Gong, W. Duan, and Y. Xu, Deep-learning density functional perturbation theory, Phys. Rev. Lett. **132**, 096401 (2024).
[43] Z. Li and S. Scandolo, Short-range order stabilizes a cubic iron alloy in Earth's inner core, Nat. Commun. **16**, 7574 (2025).
[44] Y. Fang, Y. Sun, R. Wang, F. Zheng, S. Q. Wu, C.-Z. Wang, R. M. Wentzcovitch, and K.-M. Ho, Unconventional iron-magnesium compounds at terapascal pressures, Phys. Rev. B **104**, 144109 (2021).
[45] R. Wang, Y. Sun, R. M. Wentzcovitch, F. Zheng, Y. Fang, S. Q. Wu, Z. Lin, C.-Z. Wang, and K.-M. Ho, Prediction of crystal structures and motifs in the Fe–Mg–O system at Earth's core pressures, New J. Phys. **23**, 063050 (2021).
[46] F. Zheng, Y. Sun, R. Wang, Y. Fang, F. Zhang, B. Da, S. Q. Wu, C.-Z. Wang, R. M. Wentzcovitch, and K.-M. Ho, Structure and motifs of iron oxides from 1 to 3 TPa, Phys. Rev. Mater. **6**, 043602 (2022).
[47] J. Liu, Y. Sun, C. Lv, F. Zhang, S. Fu, V. B. Prakapenka, C. Wang, K. Ho, J. Lin, and R. M. Wentzcovitch, Iron-rich Fe–O compounds at Earth's core pressures, The Innovation **4**, 100354 (2023).
[48] Y. Fang, Y. Sun, R. Wang, F. Zheng, F. Zhang, S. Q. Wu, C.-Z. Wang, R. M. Wentzcovitch, and K.-M. Ho, Structural prediction of Fe-Mg-O compounds at super-Earth's pressures, Phys. Rev. Mater. **7**, 113602 (2023).
[49] D. M. Deaven and K.-M. Ho, Molecular geometry optimization with a genetic algorithm, Phys. Rev. Lett. **75**, 288 (1995).
[50] M. S. Daw and M. I. Baskes, Embedded-atom method: Derivation and application to impurities, surfaces, and other defects in metals, Phys. Rev. B **29**, 6443 (1984).
[51] P. Brommer and F. Gähler, Potfit: Effective potentials from *ab initio* data, Model. Simul. Mater. Sci. Eng. **15**, 295 (2007).
[52] G. Kresse and J. Furthmüller, Efficient iterative schemes for *ab initio* total-energy calculations using a plane-wave basis set, Phys. Rev. B **54**, 11169 (1996).
[53] P. E. Blochl, Projector augmented-wave method, Phys. Rev. B **50**, 17953 (1994).
[54] J. P. Perdew, K. Burke, and M. Ernzerhof, Generalized gradient approximation made simple, Phys. Rev. Lett. **77**, 3865 (1996).
[55] H. J. Monkhorst and J. D. Pack, Special points for Brillouin-zone integrations, Phys. Rev. B **13**, 5188 (1976).
[56] See Supplemental Material at http://link.aps.org/supplemental/10.1103/vpqh-b5qq for convergence tests, crystal structures, a comparison between calculated and experimental pressure-dependent density, average bond length and volume plots, the volume of iron silicide compounds as a function of silicon concentration, along with phonon spectra, electronic properties, magnetic behavior, and finite-temperature thermodynamic stability, which includes Refs. [2,38,64–67].
[57] L. Stixrude, Structure of iron to 1 Gbar and 40 000 K, Phys. Rev. Lett. **108**, 055505 (2012).
[58] R. Paul, S. Hu, and V. Karasiev, Anharmonic and anomalous trends in the high-pressure phase diagram of silicon, Phys. Rev. Lett. **122**, 125701 (2019).
[59] X. Gong, D. Polsin, R. Paul, B. Henderson, J. Eggert, F. Coppari, R. Smith, J. R. Rygg, and G. Collins, X-ray diffraction of ramp-compressed silicon to 390 GPa, Phys. Rev. Lett. **130**, 076101 (2023).
[60] A. Stukowski, Visualization and analysis of atomistic simulation data with OVITO–the Open Visualization Tool, Model. Simul. Mater. Sci. Eng. **18**, 015012 (2009).
[61] A. Togo, L. Chaput, T. Tadano, and I. Tanaka, Implementation strategies in phonopy and phono3py, J. Phys.: Condens. Matter **35**, 353001 (2023).
[62] D. C. Wallace and H. Callen, Thermodynamics of crystals, Am. J. Phys. **40**, 1718 (1972).
[63] L. Vočadlo, K. S. Knight, G. D. Price, and I. G. Wood, Thermal expansion and crystal structure of FeSi between 4 and 1173 K determined by time-of-flight neutron powder diffraction, Phys. Chem. Miner. **29**, 132 (2002).
[64] Y. Dusausoy, J. Protas, R. Wandji, and B. Roques, Structure cristalline du disiliciure de fer, $FeSi_2\beta$, Struct. Sci. **27**, 1209 (1971).
[65] K. Kanematsu, Stability of crystal structure of $(Fe, V)_3M$ and $(Fe, Ni)_3M$ (M = Si, Ge, Sn) and its analysis based on rigid band model, T. Jpn. I. Met. **27**, 225 (1986).
[66] H. Kudielka, Die Kristallstruktur von Fe_2Si, ihre Verwandtschaft zu den Ordnungsstrukturen des α-(Fe, Si)-Mischkristalls und zur Fe_5Si_3-Struktur, Z. Kristallogr. - Cryst. Mater. **145**, 177 (1977).
[67] A. Osawa and T. Murata, The equilibrium diagram of the iron and silicon system, J. Japan Inst. Met **4**, 228 (1940).
[68] C. Liu, J. Shi, H. Gao, J. Wang, Y. Han, X. Lu, H.-T. Wang, D. Xing, and J. Sun, Mixed coordination silica at megabar pressure, Phys. Rev. Lett. **126**, 035701 (2021).
[69] N. Zabala, M. J. Puska, and R. M. Nieminen, Spontaneous magnetization of simple metal nanowires, Phys. Rev. Lett. **80**, 3336 (1998).
[70] A. B. Belonoshko, N. V. Skorodumova, A. Rosengren, and B. Johansson, Elastic anisotropy of Earth's inner core, Science **319**, 797 (2008).
[71] A. B. Belonoshko, N. V. Skorodumova, S. Davis, A. N. Osiptsov, A. Rosengren, and B. Johansson, Origin of the low rigidity of the Earth's inner core, Science **316**, 1603 (2007).
[72] X. Sha and R. Cohen, Elastic isotropy of $\varepsilon-$Fe under Earth's core conditions, Geophys. Res. Lett. **37**, L10302 (2010).
[73] L. Vočadlo, D. P. Dobson, and I. G. Wood, *Ab initio* calculations of the elasticity of hcp-Fe as a function of temperature at inner-core pressure, Earth Planet. Sci. Lett. **288**, 534 (2009).
[74] N. D. Mermin, Thermal properties of the inhomogeneous electron gas, Phys. Rev. **137**, A1441 (1965).

[75] S. Anzellini, A. Dewaele, M. Mezouar, P. Loubeyre, and G. Morard, Melting of iron at Earth's inner core boundary based on fast x-ray diffraction, Science **340**, 464 (2013).

[76] E. Edmund, G. Morard, M. A. Baron, A. Rivoldini, S. Yokoo, S. Boccato, K. Hirose, A. Pakhomova, and D. Antonangeli, The Fe-FeSi phase diagram at Mercury's core conditions, Nat. Commun. **13**, 387 (2022).